The Astrophysical Journal, 774:130 (8pp), 2013 September 10 doi:10.1088/0004-637X/774/2/130

THE MASS–METALLICITY RELATION OF A $z \sim 2$ PROTOCLUSTER WITH MOSFIRE

Kristin R. Kulas[1], Ian S. McLean[1], Alice E. Shapley[1], Charles C. Steidel[2], Nicholas P. Konidaris[2], Keith Matthews[2], Gregory N. Mace[1], Gwen C. Rudie[2], Ryan F. Trainor[2], and Naveen A. Reddy[3]
[1] Department of Astronomy, University of California, Los Angeles, 430 Portola Plaza, Los Angeles, CA 90095, USA; kkulas@astro.ucla.edu
[2] California Institute of Technology, MS 249-17, 1200 East California Boulevard, Pasadena, CA 91125, USA
[3] Department of Physics and Astronomy, University of California, Riverside, 900 University Avenue, Riverside, CA 92521, USA
Received 2013 June 21; accepted 2013 August 2; published 2013 August 23

ABSTRACT

We present Keck/MOSFIRE observations of the role of environment in the formation of galaxies at $z \sim 2$. Using *K*-band spectroscopy of Hα and [N II] emission lines, we have analyzed the metallicities of galaxies within and around a $z = 2.3$ protocluster discovered in the HS1700+643 field. Our main sample consists of 23 protocluster and 20 field galaxies with estimates of stellar masses and gas-phase metallicities based on the N2 strong-line metallicity indicator. With these data we have examined the mass–metallicity relation with respect to environment at $z \sim 2$. We find that field galaxies follow the well-established trend between stellar mass and metallicity, such that more massive galaxies have larger metallicities. The protocluster galaxies, however, do not exhibit a dependence of metallicity on mass, with the low-mass protocluster galaxies showing an enhancement in metallicity compared to field galaxies spanning the same mass range. A comparison with galaxy formation models suggests that the mass-dependent environmental trend we observed can be qualitatively explained in the context of the recycling of "momentum-driven" galaxy wind material. Accordingly, winds are recycled on a shorter timescale in denser environments, leading to an enhancement in metallicity at fixed mass for all but the most massive galaxies. Future hydrodynamical simulations of $z \sim 2$ overdensities matching the one in the HS1700 field will be crucial for understanding the origin of the observed environmental trend in detail.

Key words: galaxies: abundances – galaxies: clusters: general – galaxies: evolution – galaxies: formation – galaxies: high-redshift

Online-only material: color figures

1. INTRODUCTION

Galaxy clusters constitute the most massive gravitationally bound structures in the universe, making them excellent laboratories for studying galaxy formation in the most extreme environments. Galaxy properties have been demonstrated to correlate with environment in the local universe (e.g., Hogg et al. 2004; Kauffmann et al. 2004; Clemens et al. 2006; van der Wel et al. 2010; Wetzel et al. 2012). Particularly, galaxies found in the central, densest regions of clusters at $z < 1$ are typically early-type galaxies with low star formation rates (SFRs), while more active, late-type galaxies are preferentially located in the sparser edges of the cluster field. These observations suggest that environment plays a key role in the evolution of galaxies, with large-scale overdense regions appearing to foster the earliest sites of galaxy formation.

Detailed cluster studies have been conducted out to $z \sim 1$ (e.g., Holden et al. 2009; Patel et al. 2009), but there is limited information for clusters at $z > 1$ (but see, e.g., Papovich et al. 2012). Protoclusters at $z > 2$ are still in the process of forming and have not yet virialized, making them perfect for studying the origin of the environmental trends observed locally. Measuring the physical properties (e.g., stellar mass, metallicity, velocity dispersion) of protocluster galaxies will facilitate a better understanding of the processes that are relevant in dense environments and the formation times of cluster versus field galaxies, where field galaxies are defined as those not residing within an overdense region.

The metallicity of a galaxy reflects the past history of star formation, and is additionally modulated by gas inflows and outflows (Finlator & Davé 2008; Peeples & Shankar 2011; Davé et al. 2012). A relationship between stellar mass and metallicity has been well established locally, where higher-mass galaxies have larger gas-phase metallicities (Tremonti et al. 2004). This trend has been shown to hold to at least $z \sim 3$ (Erb et al. 2006; Maiolino et al. 2008), though it appears to shift toward lower metallicity at fixed mass as redshift increases. Low-redshift studies of the mass–metallicity relation (MZR) with respect to environment have demonstrated that galaxies found in overdense regions have, on average, higher metallicities compared to field galaxies of the same mass (Cooper et al. 2008; Ellison et al. 2009). Similar measurements of metallicity as a function of environment have yet to be performed at high redshift.

The newly commissioned Multi-Object Spectrometer For Infrared Exploration (MOSFIRE) instrument (McLean et al. 2012) at Keck Observatory is ideal for studying high-redshift protoclusters due to its large field of view and multiplexing capabilities. We have used MOSFIRE to collect a sizable sample of galaxies with *K*-band spectroscopy both within and outside of a redshift-space overdensity at $\langle z \rangle = 2.3$ discovered in the HS1700+643 field (Steidel et al. 2005). Environmental effects have already been detected in the HS1700 protocluster, such that protocluster galaxies appear to have average ages and stellar masses that are twice as large as those of galaxies in the surrounding, field environment. Here we consider the connections between metallicity and environment in the HS1700 field. For our sample of protocluster and field galaxies at $z \sim 2$, we have measured the important rest-frame optical diagnostic emission lines Hα and [N II] to estimate the gas-phase oxygen abundance with the N2 strong-line metallicity indicator. This dataset will make possible for the first time the examination of

the MZR for high-redshift protocluster galaxies compared to a field control sample, which will lead to a better understanding of how gas supplies are regulated during the formation of galaxies in extreme environments.

This paper is organized as follows. In Section 2 we discuss our sample selection. The observations used for this study are presented in Section 3. Section 4 describes the physical properties of the galaxies measured for this analysis. The MZR for protocluster galaxies is discussed in Section 5. In Section 6, we examine various physical processes that can explain our observational results. In Section 7, we summarize our findings and discuss their implications. A flat ΛCDM cosmology with $\Omega_m = 0.3$, $\Omega_\Lambda = 0.7$, and $H_0 = 70$ km s^{-1} Mpc^{-1} is assumed throughout.

2. SAMPLE SELECTION

The HS1700+643 field (α = 17:01:01, δ = +64:11:58) was observed as part of the Keck Baryonic Structure Survey (KBSS; Rudie et al. 2012). The KBSS was designed to explore the properties of star-forming galaxies at $z \sim 2$–3 and the connection between galaxies and the intergalactic medium (IGM) within the same cosmic volumes. As such, galaxies were targeted for spectroscopy in the fields of background, hyperluminous QSOs with high-resolution Lyα forest spectra. The galaxy spectroscopic survey was conducted with the blue arm of the Low Resolution Imaging Spectrometer (LRIS-B) on the Keck I Telescope (Oke et al. 1995; Steidel et al. 2004). Galaxies were selected based on their rest-frame ultraviolet (UV) colors using the optical photometric "BX" ($z = 2.20 \pm 0.32$) and "MD" ($z = 2.73 \pm 0.27$) criteria of Adelberger et al. (2004) and Steidel et al. (2004, 2003). Steidel et al. (2005) identified a highly significant ($\delta \sim 7$) redshift-space overdensity of galaxies at $z = 2.300$ in the 15.′3 × 15.′3 HS1700 field in the course of the KBSS. The majority of high-redshift protoclusters have been identified around radio galaxies using narrowband imaging tuned to find Lyα emitters (e.g., Venemans et al. 2007; Kodama et al. 2007). In contrast, the HS1700 protocluster consists of a serendipitous discovery of a redshift spike within a spectroscopic survey with a well-defined redshift selection function, allowing for a robust estimate of galaxy overdensity.

We selected roughly equal numbers of UV spectroscopically confirmed galaxies within and outside the redshift-space overdensity in order to conduct a detailed analysis of how environment affects the physical properties of $z \sim 2$ galaxies. We define protocluster members as galaxies at $z = 2.3 \pm 0.015$, while "field" galaxies are defined as residing outside of the redshift-space overdensity, but between $2.0 \lesssim z \lesssim 2.6$.

We used the MAGMA slitmask design tool[4] to create three separate masks, which included 24 protocluster galaxies and 21 field galaxies. A sample of 46 photometric candidates without spectroscopic redshifts were included to fill any empty slits on our three MOSFIRE masks. The stellar mass (calculated from spectral energy distribution (SED) fitting, see Section 4.1) and K_s-band magnitude distributions of our selected galaxies indicate that our MOSFIRE protocluster and field samples are representative of their respective parent UV spectroscopic protocluster and field samples. For protocluster galaxies the mean and standard deviation for stellar mass and K_s magnitude (AB) of the MOSFIRE and parent samples are, respectively, $\langle \log(M_*)_{\rm MOS} \rangle = 10.3\,M_\odot \pm 0.5$ and $\langle \log(M_*)_{\rm parent} \rangle = 10.3\,M_\odot \pm 0.5$, $\langle K_{s,\rm MOS} \rangle = 22.6 \pm 0.5$ and $\langle K_{s,\rm parent} \rangle = 22.7 \pm 0.6$. For field galaxies the mean stellar mass and K_s magnitude (AB) of the MOSFIRE and parent samples are, respectively, $\langle \log(M_*)_{\rm MOS} \rangle = 10.1\,M_\odot \pm 0.4$ and $\langle \log(M_*)_{\rm parent} \rangle = 10.2\,M_\odot \pm 0.5$, $\langle K_{s,\rm MOS} \rangle = 23.0 \pm 0.5$ and $\langle K_{s,\rm parent} \rangle = 22.9 \pm 0.7$.

[4] http://www2.keck.hawaii.edu/inst/mosfire/magma.html

3. OBSERVATIONS AND DATA REDUCTION

Both photometric and spectroscopic data are required for the analysis of the MZR. We utilized broadband ancillary photometry for our stellar mass estimates and MOSFIRE K-band spectroscopy for gas-phase metallicity. In this section we describe both datasets and the reduction processes.

3.1. Broadband Ancillary Photometry

The HS1700 field has photometric data spanning from rest-frame ultraviolet to infrared wavelengths. $U_n G\mathcal{R}$ imaging was performed on the William Herschel 4.2 m Telescope with the Prime Focus Imager. Near-infrared (near-IR) JK_s imaging was obtained on the Palomar 5.1 m Hale Telescope with the Wide Field Infrared Camera and H-band imaging was completed with HST/WFC3-F160W. Furthermore, HS1700 has photometric data from *Spitzer*/IRAC and MIPS. A complete description of the reduction of these data is contained in Reddy et al. (2012), and references therein.

3.2. MOSFIRE Spectroscopy

K-band near-IR spectroscopy of the HS1700 field was obtained using the MOSFIRE instrument on the Keck I Telescope. The MOSFIRE K-band filter is centered at 2.162 μm with a full-width at half-maximum (FWHM) of 0.483 μm. The data were acquired over six nights during MOSFIRE commissioning runs on 2012 May 6, 7, and 9 and June 2, 5, and 6. As discussed in Section 2, three separate MOSFIRE K-band masks were observed in the HS1700 field. Each individual exposure time was 3 minutes, with a total integration time of 172 minutes, 180 minutes, and 45 minutes on, respectively, masks 1, 2 and 3. All targets were observed with a slit width of 0.″7 using an AB dither sequence with 3″ offsets. The spectral resolution as determined from sky lines is ∼6 Å, which corresponds to $\Delta\upsilon \sim 80$ km s^{-1} ($R \simeq 3600$). The seeing FWHM over the six nights averaged ∼0.″5. We detected Hα for 22/24 protocluster galaxies (92%) and 15/17 field galaxies (88%) for which Hα fell within the MOSFIRE spectral format.[5]

There are six new protocluster galaxy detections, including BX759, which was previously identified as a field galaxy due to an incorrect LRIS redshift measurement and five galaxies without previously determined redshifts. In addition there are five new field galaxy detections without previously determined redshifts. We measured Hα for a total of 28 protocluster galaxies and 20 field galaxies, of which 17 protocluster galaxies and 5 field galaxies also have [N II] detections. Protocluster member BNB19 was discovered using a narrowband filter tuned to detect Lyα emission. As all other objects in the sample were selected on the basis of their rest-frame UV continuum colors, we have excluded BNB19 from this analysis, resulting in a final protocluster sample of 27 galaxies.

[5] Of the original 21 targeted field galaxies, two galaxies were determined from Hα to reside outside of the "field" redshift space and two had redshifts such that Hα fell off of the spectral format. Excluding these four objects results in a total of 17 field galaxies that were expected to have Hα detections within the MOSFIRE K-band spectral format.

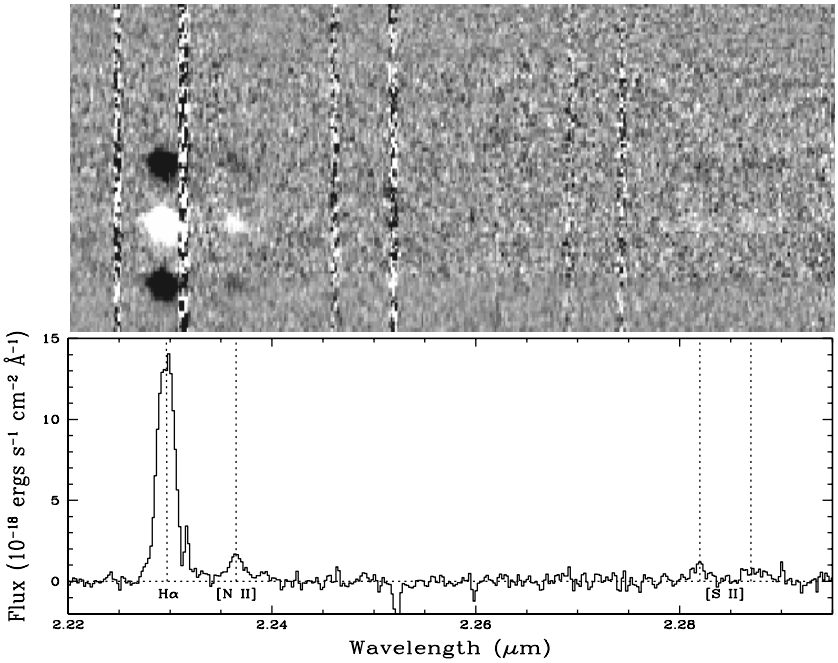

Figure 1. Top: example MOSFIRE two-dimensional spectrum for object BX490 produced from the MOSFIRE data reduction pipeline. Bottom: corresponding one-dimensional spectrum after extraction and flux calibration. In both spectra, Hα, [N II] λ6584, and [S II] $\lambda\lambda$6717, 6732 are evident from left to right.

We utilized the MOSFIRE data reduction pipeline (DRP)[6] to reduce all of the data. The DRP produces two-dimensional wavelength-calibrated, sky-subtracted, registered and combined spectra for each object, along with a corresponding inverse variance spectrum. We then extracted one-dimensional spectra from the two-dimensional reduced science and variance images using the `IRAF` procedure `apall`. This routine summed the unweighted fluxes of pixels inside of each extraction aperture. The average aperture size along the slit was 1.″4, with a range of 0.″9–2.″2. The resulting science and error spectra were placed on an absolute flux scale using observations of the A0 star HD191225 obtained during the MOSFIRE runs. Each flux-calibrated, one-dimensional spectrum was then placed in a vacuum, heliocentric frame (Figure 1).

4. PHYSICAL PROPERTIES

4.1. Stellar Masses

We estimate the stellar masses for objects in our sample as in Reddy et al. (2012), using the full rest-frame UV through IR broadband SED to find the best-fit stellar population model. A brief overview of the procedure is described here.

For stellar population modeling, we used the latest solar metallicity models of S. Charlot & G. Bruzual (in preparation) which include the Marigo & Girardi (2007) prescription for the thermally pulsating asymptotic giant branch evolution of low- and intermediate-mass stars. The broadband photometry was corrected in the optical bands for the effect of Lyα emission/absorption when the measurements were available. The K_s band was corrected for Hα nebular emission as measured from our MOSFIRE spectra. For each galaxy a constant, exponentially decreasing, and exponentially increasing star formation history (SFH) was considered. The best-fit model was determined by minimizing χ^2 with respect to the observed photometry, yielding estimates of the SFR, age, $E(B-V)$, and stellar mass. We assume a constant SFH with a minimum allowed age of 50 Myr for all of our objects. Using an exponentially decreasing or increasing SFH does not change our conclusions.

Stellar masses were estimated for 23 protocluster galaxies and all 20 field galaxies using the SED fitting procedure described above. Four protocluster galaxies (BX684, BX689, BX789, and BX935) do not have sufficient multi-wavelength broadband photometric coverage for accurate stellar mass estimates, and are not included in the following mass–metallicity analysis. The average stellar mass estimated for protocluster members, $M_* = 3.2 \times 10^{10}\,M_\odot$, is approximately twice as large as that of the field galaxy sample, $M_* = 1.9 \times 10^{10}\,M_\odot$, which suggests that the protocluster galaxies have experienced a more advanced build-up in stellar mass compared to field galaxies. This mass difference between protocluster and field galaxies was already noted by Steidel et al. (2005).

The stellar mass error for each object was determined by a Monte Carlo technique. Accordingly, each photometric data point was perturbed by a value randomly drawn from a normal Gaussian distribution, the width of which was set by the photometric error. We performed 100 trials for each object. In each trial, the best-fit SED was determined from the perturbed photometry using the same method as for the actual photometry. The stellar mass uncertainty was set equal to the standard deviation of the distribution of stellar mass measurements estimated from the artificial SEDs, utilizing a 3σ clipping method to suppress the effect of outliers. Stellar masses and corresponding errors are listed in Table 1.

4.2. Metallicities

Gas-phase metallicity reflects the entire past history of star formation, in addition to being affected by infall of metal-poor gas and outflow of metal-enriched gas (Finlator & Davé 2008; Davé et al. 2011, 2012). There are several different methods typically used for evaluating the metallicity in a galaxy. The most direct method employs the ratio between the

[6] http://code.google.com/p/mosfire/

Table 1
Physical Properties

Object	$z_{H\alpha}$	$\mathcal{R}$[a]	K_s[a,b]	M_*[c]	$F_{H\alpha}$[d]	$F_{[N\,II]}$[d]	12 + log(O/H)[e]
			Protocluster galaxies				
BNB19[f]	2.2850	23.33	···	···	6.7 ± 0.6	1.2 ± 0.2	8.48 ± 0.02
BM658	2.2939	25.29	···	0.3 ± 0.1	1.0 ± 0.1	<0.1	<8.37
BX505[g]	2.3094	25.17	22.70	4.4 ± 1.5	4.9 ± 0.2	2.3 ± 0.3	8.71 ± 0.03
BX563	2.2924	23.82	22.29	2.0 ± 0.6	11.1 ± 0.2	1.0 ± 0.2	8.30 ± 0.01
BX585	2.3085	24.71	23.35	0.5 ± 0.2	3.9 ± 0.2	<0.2	<8.18
BX649	2.2960	24.90	23.30	1.8 ± 0.5	5.6 ± 0.3	1.1 ± 0.2	8.49 ± 0.01
BX684[f]	2.2935	23.51	···	···	7.0 ± 0.3	1.1 ± 0.3	8.44 ± 0.02
BX689[f]	2.2840	23.90	···	···	8.4 ± 0.5	1.1 ± 0.2	8.39 ± 0.01
BX710	2.2960	23.96	22.03	3.6 ± 0.7	15.8 ± 0.2	1.7 ± 0.2	8.35 ± 0.01
BX711	2.2962	25.07	22.68	6.3 ± 2.0	11.0 ± 0.3	0.8 ± 0.2	8.25 ± 0.01
BX759	2.3096	24.43	23.08	1.3 ± 0.6	2.2 ± 0.3	<0.3	<8.43
BX763	2.2932	24.25	22.79	1.5 ± 0.4	7.1 ± 0.2	1.1 ± 0.2	8.44 ± 0.01
BX789[f]	2.3006	25.16	···	···	3.1 ± 0.4	<0.4	<8.36
BX810	2.2937	24.68	22.61	2.3 ± 0.8	9.9 ± 0.4	1.5 ± 0.3	8.43 ± 0.01
BX879	2.3077	23.50	22.38	1.2 ± 0.2	3.7 ± 0.3	0.7 ± 0.1	8.50 ± 0.02
BX893	2.3092	24.38	23.20	2.7 ± 1.3	1.7 ± 0.3	<0.3	<8.46
BX909	2.2949	23.73	22.27	3.7 ± 0.9	14.8 ± 0.4	1.6 ± 0.3	8.35 ± 0.01
BX913	2.2918	23.88	22.41	4.3 ± 1.9	4.4 ± 0.2	0.6 ± 0.1	8.39 ± 0.01
BX917	2.3081	24.43	21.88	7.6 ± 1.4	14.0 ± 0.5	2.1 ± 0.3	8.43 ± 0.01
BX918	2.3078	24.34	22.89	1.8 ± 0.5	5.0 ± 0.4	<0.7	<8.42
BX929	2.3081	23.83	22.88	1.9 ± 0.4	5.0 ± 0.5	<0.3	<8.18
BX935[f]	2.2860	25.18	···	···	4.2 ± 0.4	<0.3	<8.27
BX939	2.2984	24.46	22.92	0.6 ± 0.2	7.9 ± 0.4	<0.4	<8.16
BX950	2.2968	24.51	22.51	1.5 ± 0.6	3.3 ± 0.3	<0.5	<8.43
BX951	2.3067	23.17	21.89	2.7 ± 0.7	5.4 ± 0.3	1.1 ± 0.3	8.51 ± 0.02
BX984	2.2976	23.51	21.97	2.3 ± 0.6	10.3 ± 0.4	1.1 ± 0.3	8.34 ± 0.01
MD109	2.2950	25.46	23.62	1.6 ± 0.4	2.5 ± 0.2	<0.2	<8.32
MD69	2.2899	24.85	21.90	20.1 ± 1.4	9.4 ± 0.4	2.8 ± 0.2	8.60 ± 0.01
			Field galaxies				
BM568	2.3901	24.72	···	1.1 ± 0.3	2.1 ± 0.2	<0.3	<8.41
BM619	2.2668	24.04	···	1.1 ± 0.4	7.4 ± 0.2	<0.8	<8.34
BX490	2.3973	22.88	21.84	1.2 ± 0.1	30.2 ± 0.4	3.4 ± 0.2	8.36 ± 0.01
BX535	2.6382	25.16	23.46	2.9 ± 1.0	4.4 ± 0.5	<0.3	<8.27
BX575	2.4348	23.82	22.74	0.6 ± 0.2	8.8 ± 1.1	<0.6	<8.22
BX592	2.4746	24.87	···	0.8 ± 0.3	2.2 ± 0.2	<0.2	<8.33
BX604	2.2012	24.72	23.17	1.1 ± 0.3	4.6 ± 0.2	<0.4	<8.28
BX609	2.5714	24.12	23.20	0.8 ± 0.1	6.2 ± 0.5	<0.4	<8.23
BX625	2.0768	24.52	23.70	0.6 ± 0.2	3.1 ± 0.2	0.3 ± 0.1	8.31 ± 0.01
BX632	2.2353	25.12	···	1.7 ± 0.8	1.8 ± 0.3	<0.1	<8.25
BX691	2.1912	25.33	22.53	9.9 ± 1.6	9.6 ± 0.3	1.9 ± 0.3	8.50 ± 0.01
BX708	2.4006	23.92	23.46	0.7 ± 0.2	6.7 ± 0.5	<0.3	<8.11
BX713	2.1394	24.48	23.03	4.7 ± 1.8	4.9 ± 0.2	0.4 ± 0.2	8.27 ± 0.02
BX717	2.4371	24.78	23.74	0.8 ± 0.4	3.7 ± 0.2	<0.3	<8.24
BX752	2.4016	24.86	22.69	4.4 ± 1.0	8.7 ± 0.7	2.4 ± 0.3	8.58 ± 0.02
BX772	2.3436	24.96	23.02	3.6 ± 0.6	4.6 ± 0.4	<0.3	<8.25
BX801	2.0393	24.11	···	1.0 ± 0.4	9.7 ± 0.3	<0.9	<8.31
BX880	2.4381	24.98	···	0.6 ± 0.4	1.0 ± 0.1	<0.1	<8.40
BX881	2.1822	24.99	23.95	0.4 ± 0.2	1.3 ± 0.2	<0.7	<8.76
MD77	2.5091	24.86	22.94	0.8 ± 0.3	7.7 ± 0.4	<0.3	<8.13

Notes.
[a] Magnitudes are on the AB system.
[b] Objects with no reported K_s magnitude are not detected down to a 3σ limit of 24.05 AB.
[c] Stellar mass in units of $10^{10}\ M_{\odot}$.
[d] Emission-line flux and uncertainty in units of 10^{-17} erg s^{-1} cm^{-2}.
[e] Errors listed are determined solely from propagation of the emission-line flux uncertainty measurements and do not include the systematic uncertainty in the N2 calibration.
[f] Object not included in the MZR analysis.
[g] Gas-phase oxygen abundance above solar.

[O III] λ4363 auroral line and lower excitation lines such as [O III] λλ5007, 4959, which allows a direct measurement of the oxygen abundance via the electron temperature (T_e) of the gas. However, [O III] λ4363 is typically too weak to detect in high-redshift galaxies. Due to the difficulties in measuring the gas-phase metallicity with the direct method, empirical calibrations have been developed which fit a relationship between the direct T_e method and strong-line ratios in H II regions.

To calculate the metallicity, we used the N2 indicator, N2 ≡ log([N II]/Hα), which traces gas-phase oxygen abundance (Pettini & Pagel 2004). Since Hα and [N II] are close in wavelength, systematic uncertainties in N2 from dust extinction, flux calibration, and instrumental effects are insignificant. However, one drawback of N2 is the saturation of this ratio above solar metallicity, making it an unreliable tracer of metallicity in this regime. To calculate N2, we measured the flux for Hα and [N II] simultaneously using a fixed central wavelength and FWHM based on the best-fit parameters for Hα, which is the brighter line. A combined fit was obtained for both emission lines by fitting Gaussian profiles using the IRAF task, splot.

We employed a Monte Carlo technique to measure the uncertainties in the emission-line centroid, flux, and FWHM. For each object, 500 fake spectra were created by perturbing the flux at each wavelength of the true spectrum by a Gaussian random number with the standard deviation set by the level of the 1σ error spectrum. Line measurements were obtained from the fake spectra in the same manner as the actual data. The standard deviation of the distribution of measurements from the artificial spectra was adopted as the error on the centroid, flux, and FWHM. For objects with no detected [N II] emission, 500 simulated spectra were created in the same manner as described above to measure upper limits. The flux was summed at the nominal position of [N II] over an interval defined by the extent of the measured Hα emission line above the continuum in each simulated spectra. We defined the 1σ upper limit as the standard deviation of the distribution of the calculated flux from the artificial spectra.

To determine the gas-phase oxygen abundance from N2, we used the calibration from Pettini & Pagel (2004), which was established from a linear fit to a large sample of local extragalactic H II regions with both N2 measurements and direct T_e-based oxygen abundance estimates. According to this calibration,

$$12 + \log(\mathrm{O/H}) = 8.90 + 0.57 \times \mathrm{N2}. \quad (1)$$

This relation has an inherent 1σ dispersion of ±0.18 dex, which is the dominant source of error in our metallicity measurements for individual galaxies. It should be noted that since the conversion between N2 and gas-phase oxygen abundance was calibrated from a sample of low-redshift galaxies, this conversion may not be valid for high-redshift galaxies (Shapley et al. 2005; Liu et al. 2008). For example, unknown differences in H II-region physical conditions may pertain at high redshift, extending to the electron density, ionization parameter and nitrogen-to-oxygen abundance. These evolutionary differences may lead to both a possible systematic offset and increased scatter in the N2 indicator. However, the differential nature of this study between protocluster and field galaxies at $z \sim 2$ mitigates the importance of a possible divergence between low- and high-redshift objects. The uncertainty in the calibration, though, may result in a 1σ dispersion larger than 0.18 dex at higher redshift. Metallicities and uncertainties are listed for each object in Table 1. The metallicity uncertainties stated in Table 1 were estimated solely from propagation of the emission-line flux errors as calculated from the Monte Carlo method described above. These errors do not include the systematic uncertainty in the N2 calibration.

5. MASS–METALLICITY RELATION

The existence of a correlation between the mass of a galaxy and the gas-phase metallicity was first noted in the late 1970s by Lequeux et al. (1979). Since then the correlation between metallicity and stellar mass has been firmly established for nearby galaxies and traced out to $z \sim 3$ for star-forming galaxies (Tremonti et al. 2004; Erb et al. 2006; Kewley & Ellison 2008; Mannucci et al. 2009). The source of this relation, however, remains uncertain. Numerous models have been created to explain the origin and observed evolution of the MZR (e.g., Finlator & Davé 2008; Oppenheimer & Davé 2008; Davé et al. 2012). Observations of the MZR provide the much needed constraints for these galaxy formation models in order to understand how the gas supply is regulated in galaxies.

At $z \sim 0$ it has been demonstrated that galaxies found in overdense regions have enhanced gas-phase metallicities compared to field galaxies at the same stellar mass (Cooper et al. 2008; Ellison et al. 2009). At higher redshift, the relationship among mass, metallicity, and environment has not been well studied due to small sample sizes and a lack of robust environmental measurements. Examining the MZR with respect to environment provides a unique probe into how baryons cycle in and out of galaxies, and offers additional constraints on galaxy formation models. Our measurements of gas-phase metallicities of galaxies within and surrounding the HS1700 protocluster present a special opportunity for connecting metallicity and environment at early times.

Figure 2 shows the gas-phase metallicity versus stellar mass for protocluster (in red) and field galaxies (in black) in our sample. Downward arrows indicate 1σ upper limits. The data from Erb et al. (2006) are also shown (in blue) in Figure 2. These authors constructed the MZR based on the N2 indicator for a sample of 87 star-forming galaxies at $\langle z \rangle = 2.3$ binned into composite spectra by stellar mass. In contrast, the MOSFIRE data points are from *individual* objects. Measurements of individual galaxies are important for understanding the inherent scatter of the MZR, in addition to enabling a more direct, object-by-object, comparison to other physical properties such as SFRs. The dotted curve is the MZR derived by Erb et al. (2006) using the N2 indicator for ∼53,000 Sloan Digital Sky Survey (SDSS) galaxies (Tremonti et al. 2004) after the application of a downward shift of 0.56 dex as implied by the Erb et al. (2006) data. The protocluster and field galaxies are distributed around the fit, with the majority appearing to fall below the Erb et al. (2006) trend, which corresponds to a lower metallicity for a given stellar mass. The dashed horizontal line indicates solar metallicity, where the N2 indicator saturates. One of our objects, BX505, has a measured gas-phase metallicity above solar.

To detect differences between the protocluster and field galaxy samples, we binned the galaxies by stellar mass and constructed composite MOSFIRE spectra for each bin. A caveat related to using composite spectra is that they do not reflect the scatter among the individual points. However, given that more than half of the objects in the sample have measured upper limits in [N II]/Hα, composite spectra offer the most robust method to examine the average [N II]/Hα ratio and corresponding metallicity in each bin. We created low- and high-mass bins for both protocluster and field samples. These bins

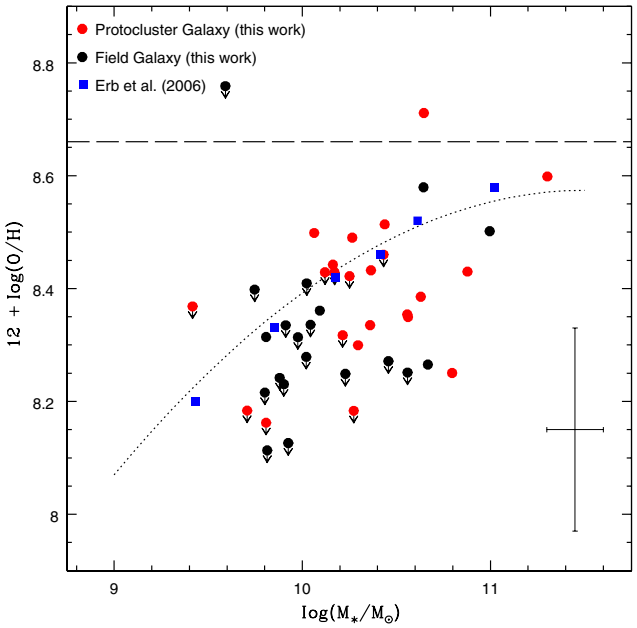

Figure 2. MZR for the protocluster (red circles) and field (black circles) galaxy samples at $z \sim 2$ using the N2 indicator. Downward arrows represent 1σ upper limits in [N II] to Hα. The dashed horizontal line represents solar abundance, where N2 saturates. The blue squares are from Erb et al. (2006), indicating star-forming galaxies at $\langle z \rangle = 2.3$, based on composite spectra binned by stellar mass. The dotted curve is the MZR based on ~53,000 SDSS galaxies after a downward shift of 0.56 dex, as in Erb et al. (2006). Error bars are shown in the lower-right corner, indicating the average errors in stellar mass and gas-phase metallicity. The metallicity error is dominated by the calibration uncertainty from the N2 indicator.

(A color version of this figure is available in the online journal.)

were designed so that the average mass was roughly equivalent for the corresponding protocluster and field subsamples at both low and high mass. For the protocluster sample, there are 6 galaxies in the lower-mass bin and 17 in the higher-mass bin. For the field sample, there are 14 galaxies in the lower-mass bin and 6 in the higher-mass bin. To create the composite spectrum for each bin, we first shifted each individual spectrum into the rest frame using the redshift calculated from the observed Hα wavelength. Next we converted each spectrum from F_λ to L_λ using the monochromatic luminosity distance to remove any redshift dependence on the observed flux. Finally, the IRAF task `scombine` was used to compute the average at each wavelength of the rest-frame spectra with a minimum/maximum pixel rejection (Figure 3). Hα and [N II] were measured and the corresponding N2-based metallicities estimated for each composite spectrum in the same manner as described for the individual galaxies.

Figure 4 shows the gas-phase oxygen abundance calculated with the N2 indicator from each mass bin plotted versus the corresponding mean stellar mass. The horizontal bars show the range of stellar masses in each bin. The metallicity measurement errors were calculated from a Monte Carlo approach taking into account both sample variance and stellar mass uncertainties. We generated 500 realizations of the low- and high-mass composite spectra for both the protocluster and field samples. In each realization, in order to account for the error in stellar mass, the stellar mass of each galaxy was randomly perturbed according to a Gaussian distribution with the width set by the 1σ stellar mass error. Both samples of protocluster and field galaxies were then sorted by the perturbed stellar mass, and divided into low- and high-mass bins as defined by the mass ranges of the original composite bins. Despite using perturbed masses, we found that the numbers of objects in each mass bin were typically consistent with the numbers in the original, unperturbed bins. Finally, to account for sample variance, the protocluster and field galaxies in each mass bin were bootstrap resampled. The vertical metallicity error bars include the error from the N2 calibration of 12 + log(O/H), reduced by $N^{1/2}$ where N is the number of objects in the original composite spectrum, as well as the uncertainties in the measurements of the Hα and [N II] fluxes from the bootstrap Monte Carlo method. The field galaxies in Figure 4 show a clear trend similar to the one in Erb et al. (2006), but shifted down by ~0.1 dex in metallicity at fixed stellar mass. To quantify the significance of this difference, we applied best-fit linear regressions to both the field galaxies and the Erb et al. (2006) data. The parameters of the linear regressions to the Erb et al. (2006) and field galaxy datasets are consistent within the 1σ errors, demonstrating that the two datasets are not significantly different.

Figure 4 also indicates that there is no strong correlation between mass and metallicity for protocluster galaxies, with both mass bins having approximately the same measured gas-phase metallicity. A comparison between protocluster and field trends reveals that the high-mass protocluster and field bins are consistent with each other in metallicity. It is at lower masses that the two samples diverge, with the protocluster metallicity notably higher than that of the field sample.

6. DISCUSSION

In this section, we consider physical mechanisms that may give rise to the observed $z \sim 2$ trends between environment and metallicity in the HS1700 field. Davé et al. (2011) utilize cosmological hydrodynamical simulations of galaxy formation to investigate how inflows, outflows, and star formation affect the metal content and gas fraction in a galaxy over cosmic time. Specifically, these authors examine the effect of local environment on the metallicities of simulated galaxies. In Davé et al. (2011) environment is defined by measuring the local galaxy density in a 1 h^{-1} Mpc top-hat sphere. Galaxies at densities greater than 0.5σ above the mean are considered to reside in high-density regions. The Davé et al. (2011) simulations reveal an enhancement of the mean metallicity for objects found in overdense regions at $z = 0$ using either "momentum-driven winds" or "no-winds" models. Finlator & Davé (2008) also advance the model of momentum-driven winds to reproduce the MZR from Tremonti et al. (2004) at $z \sim 0$ and Erb et al. (2006) at $z \sim 2$. Outflows have been shown to be ubiquitous for $z \sim 2$–3 UV-selected star-forming galaxies (Pettini et al. 2001; Shapley et al. 2003; Steidel et al. 2010). Therefore, the no-winds model clearly does not provide an accurate description of these systems, leaving the momentum-driven scenario. With this prescription for winds, the enhancement in metallicity disappears in galaxies at masses greater than $10^{11}\ M_\odot$ (see Figure 14 in Davé et al. 2011).

Steidel et al. (2005) established that the HS1700 protocluster corresponds to a physical overdensity of $\Delta\rho/\langle\rho\rangle \sim 2$. Qualitatively, the momentum-driven winds model can replicate the MZR of the protocluster members if we assume that the Davé et al. (2011) results for environmental dependence exist at $z \sim 2$ for an overdensity similar to that found in HS1700. In detail, Davé et al. use a different density estimator, which prevent us from making a quantitative comparison. In addition, these authors indicate that the environmental metallicity enhancement disappears at a stellar mass that is a factor of two more massive

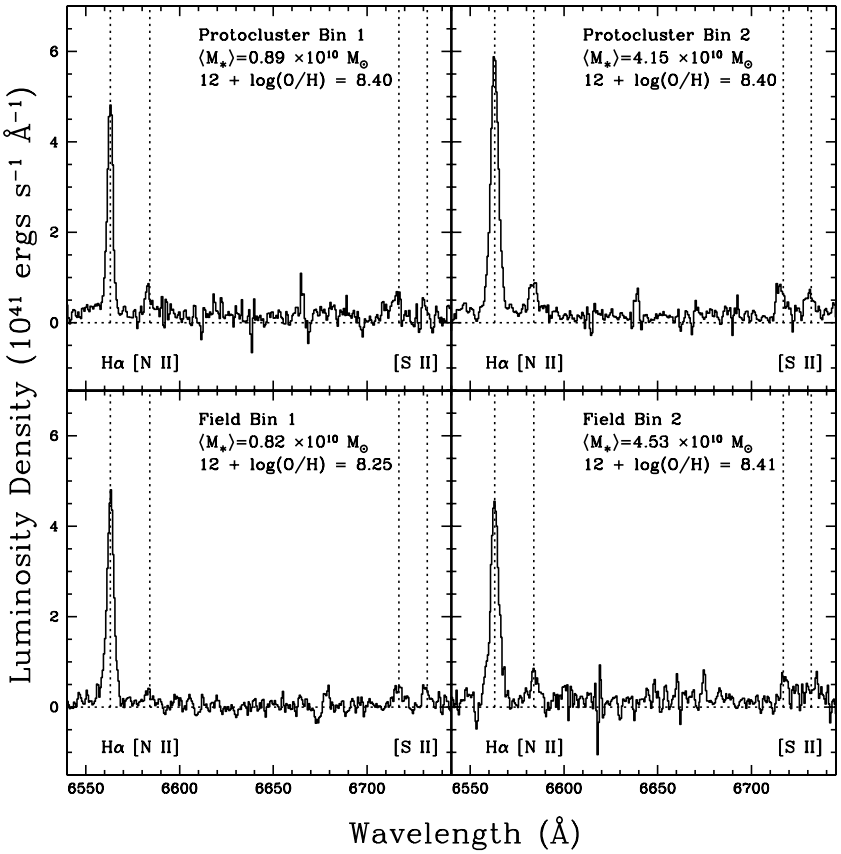

Figure 3. Rest-frame composite spectra for each protocluster and field galaxy bin. The first and second columns are, respectively, the low- and high-mass bins. The top row features protocluster galaxy composites and the bottom row shows the field galaxy composites. From left to right, Hα, [N II] λ6584, and [S II] $\lambda\lambda$6717, 6732 are marked on each spectrum. In addition, the mean stellar mass and metallicity are labeled for each bin.

than suggested in our results. This discrepancy may be attributed to the difference in redshift between the Davé et al. simulated objects at $z = 0$ and our galaxies at $z \sim 2$ if the transition for the disappearance of the metallicity enhancement occurs at lower masses during earlier epochs.

Davé et al. (2011) suggest that the metallicity enhancement in overdense environments at $z = 0$ may be due to the differentially higher enrichment of intergalactic gas in such regions, resulting in cluster galaxies accreting additional metals compared with field galaxies. At $z \sim 2$, however, when the IGM has had less time for differential enrichment, the significance of this effect is unclear. Furthermore, the observed metallicity enhancement for HS1700 protocluster galaxies exhibits a mass dependence, with a larger metallicity offset at lower stellar masses. This mass dependence indicates that a general enhancement of the metallicity of infalling gas in an overdensity cannot alone explain the environmental MZR trend we observe. Davé et al. (2011) turn to the results of Oppenheimer & Davé (2008) to explain the origin of a mass-dependent environmental trend in metallicity.

As reported by Oppenheimer & Davé (2008), environment is a primary factor determining how far winds can carry metals, and how long it will take for the metals to fall back into the galaxy and be "recycled." Specifically, these authors demonstrate in their simulation that the timescale for metals to be recycled is inversely correlated with environmental density, such that metals are recycled more rapidly in denser environments (see panel (b) of Figures 12 and 14 in Oppenheimer & Davé 2008). Accordingly, low- to intermediate-mass protocluster galaxies will recycle their metals more efficiently due to residing in an overdense environment, compared with field galaxies of the same mass. However, at the highest masses, wind recycling is so effective that all galaxies re-accrete their ejected metals quickly regardless of environment. These mass-dependent results of wind recycling are reflected qualitatively in our Figure 4, with an offset between the protocluster and field MZRs at lower stellar mass, but not at higher stellar mass. In detail, however, the actual high-mass threshold at which the environmental effect disappears must also be matched. Models of galactic outflows at $z \sim 2$ including environments similar to the HS1700 overdensity are needed to investigate if the environmental dependence of wind recycling is a viable explanation for the MZR trends we observe.

7. SUMMARY

In this paper we utilize Keck/MOSFIRE data to examine the gas-phase oxygen abundance of 23 protocluster and 20 field galaxies with respect to stellar mass in the HS1700 field. Metallicities were measured from the [N II]/Hα ratio, while stellar masses were estimated from stellar population modeling of rest-frame UV through IR SEDs. We first examined the correlation between stellar mass and metallicity for each *individual* galaxy and conclude that the sample is distributed around the Erb et al. (2006) result, with the majority of galaxies found below this trend. We then created composite spectra to study the MZR for protocluster and field galaxies separately. The field composite datapoints are slightly lower in metallicity but consistent with previous studies of $z \sim 2$ star-forming galaxies within the 1σ errors. The protocluster galaxies,

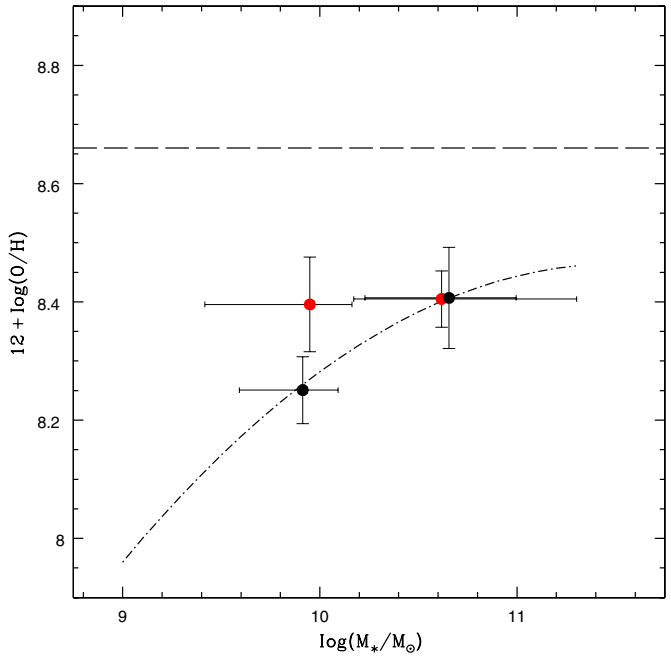

Figure 4. MZR for protocluster and field galaxies binned by stellar mass. The horizontal bars represent the mass range in each bin. The vertical error bars represent the 1σ error from the emission-line measurements and the N2 calibration. The dotted line is the same as from Erb et al. (2006) except that it has been shifted downward by 0.67 dex from the Tremonti et al. (2004) fit instead of 0.56 dex. The field galaxies appear to follow the trend presented in Erb et al. (2006), while the protocluster galaxies show no strong correlation with mass and metallicity, with both protocluster galaxy mass bins having approximately the same measured gas-phase metallicity.

(A color version of this figure is available in the online journal.)

however, demonstrate no correlation between metallicity and stellar mass. In detail, the protocluster and field high-mass bins for both samples are consistent, while the low-mass protocluster bin is measured to have a higher metallicity than that of the corresponding low-mass field bin.

Recent cosmological hydrodynamical simulations of galaxy formation suggest that winds carrying metals will recycle more efficiently back to the host galaxy in an overdense environment, which may lead to cluster galaxies having enhanced gas-phase metallicity at moderate stellar mass. At high stellar masses, though, wind recycling is so effective that all galaxies re-accrete their ejected metals quickly. Galaxy formation models featuring an environment similar to that in HS1700 at $z \sim 2$ need to be investigated to understand if environmental dependence of enriched infall caused by wind recycling provides a viable explanation for our observations. This work represents the first analysis of an environmental dependence of the MZR at $z \sim 2$, a crucial step toward understanding how gas reservoirs are regulated in extreme environments during galaxy formation.

MOSFIRE was developed by the consortium of the University of California, Los Angeles, the California Institute of Technology, the University of California, Santa Cruz and the W. M. Keck Observatory. Funding was provided by a grant from the National Science Foundation's Telescope System Instrumentation Program and by a generous donation from Gordon and Betty Moore to the Keck Observatory. We thank the entire MOSFIRE team, whose dedication and hard work made this project possible. We also gratefully acknowledge the outstanding support of the entire Keck Observatory staff during commissioning, especially Marc Kassis, Greg Wirth and Al Honey. A.E.S. acknowledges support from the David and Lucile Packard Foundation. N.P.K. acknowledges support from the NSF grant 1106171. Additionally, we acknowledge Romeel Davé for insightful conversations. Finally, we wish to extend special thanks to those of Hawaiian ancestry on whose sacred mountain we are privileged to be guests. Without their generous hospitality, most of the observations presented herein would not have been possible.

REFERENCES

Adelberger, K. L., Steidel, C. C., Shapley, A. E., et al. 2004, ApJ, 607, 226
Clemens, M. S., Bressan, A., Nikolic, B., et al. 2006, MNRAS, 370, 702
Cooper, M. C., Tremonti, C. A., Newman, J. A., & Zabludoff, A. I. 2008, MNRAS, 390, 245
Davé, R., Finlator, K., & Oppenheimer, B. D. 2011, MNRAS, 416, 1354
Davé, R., Finlator, K., & Oppenheimer, B. D. 2012, MNRAS, 421, 98
Ellison, S. L., Simard, L., Cowan, N. B., et al. 2009, MNRAS, 396, 1257
Erb, D. K., Shapley, A. E., Pettini, M., et al. 2006, ApJ, 644, 813
Finlator, K., & Davé, R. 2008, MNRAS, 385, 2181
Hogg, D. W., Blanton, M. R., Brinchmann, J., et al. 2004, ApJL, 601, L29
Holden, B. P., Franx, M., Illingworth, G. D., et al. 2009, ApJ, 693, 617
Kauffmann, G., White, S. D. M., Heckman, T. M., et al. 2004, MNRAS, 353, 713
Kewley, L. J., & Ellison, S. L. 2008, ApJ, 681, 1183
Kodama, T., Tanaka, I., Kajisawa, M., et al. 2007, MNRAS, 377, 1717
Lequeux, J., Peimbert, M., Rayo, J. F., Serrano, A., & Torres-Peimbert, S. 1979, A&A, 80, 155
Liu, X., Shapley, A. E., Coil, A. L., Brinchmann, J., & Ma, C. 2008, ApJ, 678, 758
Maiolino, R., Nagao, T., Grazian, A., et al. 2008, A&A, 488, 463
Mannucci, F., Cresci, G., Maiolino, R., et al. 2009, MNRAS, 398, 1915
Marigo, P., & Girardi, L. 2007, A&A, 469, 239
McLean, I. S., Steidel, C. C., Epps, H. W., et al. 2012, Proc. SPIE, 8446, 84460J
Oke, J. B., Cohen, J. G., Carr, M., et al. 1995, PASP, 107, 375
Oppenheimer, B. D., & Davé, R. 2008, MNRAS, 387, 577
Papovich, C., Bassett, R., Lotz, J. M., et al. 2012, ApJ, 750, 93
Patel, S. G., Kelson, D. D., Holden, B. P., et al. 2009, ApJ, 694, 1349
Peeples, M. S., & Shankar, F. 2011, MNRAS, 417, 2962
Pettini, M., & Pagel, B. E. J. 2004, MNRAS, 348, L59
Pettini, M., Shapley, A. E., Steidel, C. C., et al. 2001, ApJ, 554, 981
Reddy, N. A., Pettini, M., Steidel, C. C., et al. 2012, ApJ, 754, 25
Rudie, G. C., Steidel, C. C., Trainor, R. F., et al. 2012, ApJ, 750, 67
Shapley, A. E., Coil, A. L., Ma, C., & Bundy, K. 2005, ApJ, 635, 1006
Shapley, A. E., Steidel, C. C., Pettini, M., & Adelberger, K. L. 2003, ApJ, 588, 65
Steidel, C. C., Adelberger, K. L., Shapley, A. E., et al. 2003, ApJ, 592, 728
Steidel, C. C., Adelberger, K. L., Shapley, A. E., et al. 2005, ApJ, 626, 44
Steidel, C. C., Erb, D. K., Shapley, A. E., et al. 2010, ApJ, 717, 289
Steidel, C. C., Shapley, A. E., Pettini, M., et al. 2004, ApJ, 604, 534
Tremonti, C. A., Heckman, T. M., Kauffmann, G., et al. 2004, ApJ, 613, 898
van der Wel, A., Bell, E. F., Holden, B. P., Skibba, R. A., & Rix, H.-W. 2010, ApJ, 714, 1779
Venemans, B. P., Röttgering, H. J. A., Miley, G. K., et al. 2007, A&A, 461, 823
Wetzel, A. R., Tinker, J. L., & Conroy, C. 2012, MNRAS, 424, 232